# Uncovering the origin of Magnetic Moment Enhancement in Fe–Co–Ir Alloys via High-Throughput XMCD

Takahiro Yamazaki[1,*], Takahiro Kawasaki[1], Alexandre Lira Foggiatto[1], Ryo Toyama[2], Kentaro Fuku[1], Varun Kumar Kushwaha[2], Yoshinori Kotani[3], Takuo Ohkochi[3,4], Kotaro Higashi[3], Naomi Kawamura[3], Yuya Sakuraba[2], Yuma Iwasaki[5], Masato Kotsugi[1]

[1] *Department of Material Science and Technology, Tokyo University of Science, 6-3-1 Niijuku, Katsushika, Tokyo 125-8585, Japan*
[2] *Research Center for Magnetic and Spintronic Materials (CMSM), National Institute for Materials Science (NIMS), 1-2-1 Sengen, Tsukuba, Ibaraki 305-0047, Japan*
[3] *Japan Synchrotron Radiation Research Institute, Sayo, Hyogo 679-5198, Japan*
[4] *Laboratory of Advanced Science and Technology for Industry, University of Hyogo, Hyogo 678-1205, Japan*
[5] *Center for Basic Research on Materials (CBRM), National Institute for Materials Science (NIMS), 1-1 Namiki, Tsukuba, Ibaraki 305-0044, Japan*
*Corresponding author: takahiro.yamazaki@rs.tus.ac.jp

## Abstract

High-magnetization ferromagnets play a crucial role in advancing spintronics, magnetic sensing, and high-density data storage technologies. Fe–Co–Ir alloys, previously identified through machine learning to potentially surpass the Slater-Pauling limits for transition-metal magnets, present a valuable platform for uncovering the mechanisms behind their enhanced magnetic properties. This study investigates the influence of Ir doping on the element-specific magnetic moments by high-throughput X-ray Magnetic Circular Dichroism (XMCD) techniques using both soft and hard X-rays on Fe–Co–Ir single-crystal composition-spread thin films. A single-crystal composition-spread thin film of $(Fe_{75}Co_{25})_{100-x}Ir_x$ ($x$ = 0–11 at%) was fabricated on a MgO(100) substrate using a combinatorial sputtering technique, enabling a systematic analysis of compositional variations. XMCD measurements revealed that Ir doping enhances the magnetic moments of Fe, Co, and Ir, with a particular emphasis on the orbital contribution of Fe and Ir. These experimental findings are supported by *ab-initio* calculations, which highlight increased electron localization and stronger spin-orbit coupling between Ir 5*d* electrons and Fe/Co 3*d* electrons as the primary mechanisms behind the enhanced magnetization. This study provides a deeper understanding of the electronic and magnetic moments in Fe–Co–Ir alloys, offering valuable insights for the development of next-generation ferromagnetic materials optimized for advanced technological applications.

**Keywords**: ferromagnetic materials, soft and hard X-ray magnetic circular dichroism (XMCD), element-specific analysis, magnetic moments, Fe–Co–Ir alloys, combinatorial sputtering, *ab-initio* calculations, high-throughput measurements

## I. INTRODUCTION

High-magnetization ferromagnets are indispensable in the evolution of spintronics, magnetic sensing, and high-density data storage technologies, where their precise control over spin dynamics remains a fundamental component of next-generation device development [1−4]. Among these materials, the binary $Fe_{75}Co_{25}$ alloy stands out due to the strongest magnetic moments among the 3*d* transition metal magnets based on the Slater-Pauling rule [5], combined with its high Curie temperature and robust phase stability [6−10]. To further enhance magnetization, epitaxially grown films with their controlled crystal structures and lattice parameters have demonstrated remarkably high magnetization and offering optimal conditions for magnetic enhancement [11−14]. For instance, ultrathin epitaxial films of Fe–Co–Mn systems exhibit large magnetization [13,14], though this has proven difficult to achieve in non-epitaxial films or bulk materials [10]. Accurately predicting, validating, and fully understanding the mechanisms driving the magnetic properties of Fe–Co based alloys, especially given the complexities of multi-component systems, is a significant scientific challenge.

Recent advances in computational techniques, such as integration of machine learning and *ab-initio* calculations, have greatly accelerated the discovery of new materials from vast compositional spaces [15–23]. For example, Iwasaki *et al.* predicted magnetic moments in Fe–Co–Ir–Pt alloys that exceed those of conventional binary Fe–Co alloys through an autonomous exploration framework, which was successfully validated by fabricating magnetron-sputtered $(Fe_{75}Co_{25})_{97.5}Ir_{2.5}$ polycrystalline films [21]. However, the use of polycrystalline films and macroscopic magnetization measurement via vibrating-sample magnetometer (VSM) limited the detailed investigation of intrinsic magnetic properties. To overcome these limitations, advanced experimental approaches for quantitative determination of microscopic magnetic moments using single-crystal films are needed to validate these predictions and provide deeper insights into the fundamental magnetic mechanisms.

The addition of 5*d* transition metals plays a critical role in tuning the magnetic properties of transition-metal based alloys [21, 24–35]. Toyama *et al.* demonstrated intriguing phenomena in single-crystal Fe–Co–Ir thin films, such as anisotropic magnetoresistance (AMR) effect, anomalous Hall effect (AHE), and anomalous Nernst effect (ANE) [24, 25]. Similarly, other alloy systems like Fe–Pt–Ir [30] and Fe–Au [31], Ni–Pd [32] have shown unique magnetic behaviors, such as perpendicular magnetic anisotropy, antisymmetric exchange interaction and enhanced magnetic moments, respectively. These effects, largely driven by spin-orbit coupling, result in significant changes to both electronic structure and magnetism. Despite these advances, the interplay between the electronic structure modifications induced by 5*d* elements and the magnetic states arising from 3*d* electron behavior remains insufficiently understood.

To overcome the challenges in accurately analyzing magnetic properties, we have implemented a high-throughput approach utilizing X-ray Magnetic Circular Dichroism (XMCD) on compositionally graded thin films. Combinatorial synthesis is an efficient method for rapidly discovering new materials, enabling the systematic investigation of extensive material libraries [36–39]. Combined with XMCD technique, it provides a detailed, element-specific understanding of magnetic moments by distinguishing between orbital and spin contributions to overall magnetization [40–43]. By using soft X-rays for 3*d* transition metals such as Fe and Co, and hard X-rays for heavy metal like Ir, we can achieve a detailed understanding of the individual elements' contributions to magnetic behavior. Unlike earlier studies on non-single-crystal films [23], our work focuses on single-crystal Fe–Co–Ir thin films, offering a more controlled environment for probing the mechanisms underlying magnetic moment enhancements. This approach provides clearer insights into the intricate atomic interactions responsible for the observed magnetic improvements.

This study employs cutting-edge X-ray Magnetic Circular Dichroism (XMCD) techniques to investigate the role of Ir doping in enhancing the magnetic properties of single-crystal composition-spread thin films of $(Fe_{75}Co_{25})_{100-x}Ir_x$ ($x$ = 0–11 at%). Using a combinatorial sputtering system, we systematically explored composition-dependent magnetic behaviors. Through the high-throughput XMCD measurements utilizing both soft and hard X-rays, we captured element-specific magnetic moments, uncovering how Ir doping intricately influences the spin and orbital contributions to magnetization. Complemented by *ab-initio* calculations, our analysis provides detailed insights into the electronic structure and magnetic moments responsible for the observed enhancements in magnetization. These experimental and theoretical approaches advance the understanding of electronic and magnetic interactions in Fe–Co–Ir alloys, contributing to the development of next-generation ferromagnetic materials optimized for technological applications.

## II. METHODS

### A. Sample preparation

Single-crystal composition-spread thin film of $(Fe_{75}Co_{25})_{100-x}Ir_x$ ($x$ = 0–11 at%) was prepared on MgO(100) substrate using a combinatorial sputtering system (CMS-A6250X2, Comet Co., Ltd.), following methodologies reported in prior studies [24,25,44]. This approach allows the acquisition of a composition gradient within a single film (Fig. 1(a)), enabling high-throughput analysis by numerous measurement points. For the composition-spread film, Fe and Co targets were co-sputtered, with power setting adjusted to yield a 0.44 nm-thick film corresponding to the $Fe_{75}Co_{25}$ composition. To achieve a wedge-shaped deposition, a linear moving mask was used, varying the thickness gradient from 0.00 to 0.06 nm over a 7 mm width. The substrate was then rotated 180°, and a similar wedge-shaped Ir layer was deposited using the same mask, ensuring a complementary gradient. The process was repeated 60 times, resulting in a 30 nm thick $(Fe_{75}Co_{25})_{100-x}Ir_x$ film. The sputtering process was conducted at room temperature in an argon atmosphere at a pressure of 0.8 Pa. Post-deposition, the film was subjected to vacuum annealing at 653 K for 30 minutes to promote uniform composition distribution. To prevent oxidation, a 2-nm thick Ru capping layer was subsequently deposited. The compositional analysis using fluorescence X-ray analysis (ZSX Primus II, Rigaku) confirmed a gradient from $Fe_{75.4}Co_{24.6}$ at one end of the film to $(Fe_{76.1}Co_{23.9})_{89.0}Ir_{11.0}$ at the opposite end, establishing a linearly continuous compositional gradient across a span of 7 nm. The phase transition from $A2$-disordered to $B2$-ordered $Fe_{75}Co_{25}$–Ir structure was confirmed with Ir concentration at least from 2.1 at% [24], with Ir atoms occupying specific lattice sites, shown in blue sites as shown in Fig. 1(b).

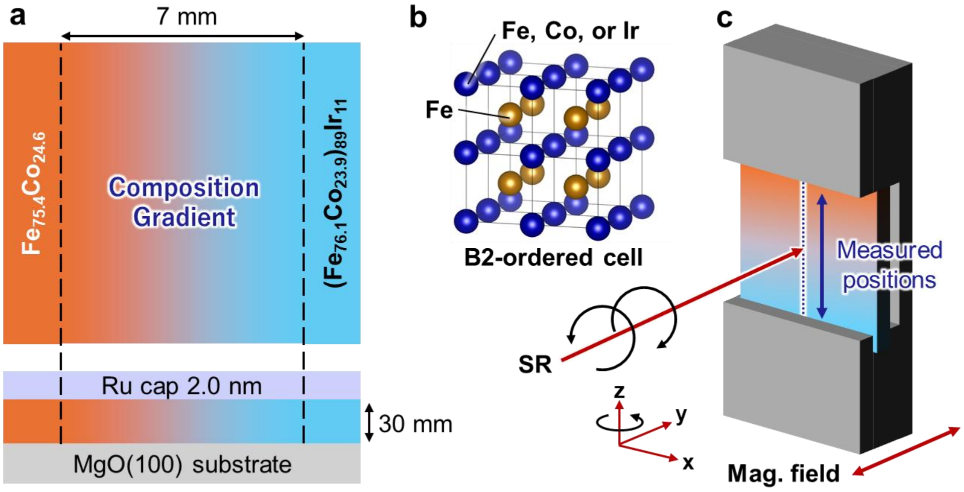

FIG. 1. (a) Schematic illustration of the fabricated compositionally graded $Fe_{75}Co_{25}$–Ir film, exhibiting a gradient in composition from $Fe_{75.4}Co_{24.6}$ to $(Fe_{76.1}Co_{23.9})_{89.0}Ir_{11.0}$ across a 7 mm span. The film is capped with a 2.0 nm Ru layer and is deposited on an MgO(100) substrate. (b) Schematic of the $B2$-ordered crystal structure in the Fe–Co–Ir alloy, highlighting the atomic arrangement within the alloy. (c) Experimental setup for X-ray Magnetic Circular Dichroism (XMCD) measurements using a synchrotron X-ray source generated by a twin helical undulator, with measured positions indicated along the compositional gradient of the film.

### B. Soft and hard XMCD measurements

XMCD measurements were performed to investigate the element-specific electronic structure and magnetic moments of the Fe, Co, and Ir elements in the $(Fe_{75}Co_{25})_{100-x}Ir_x$ ($x$ = 0–11 at%) alloy. These measurements were conducted at the SPring-8 synchrotron facility in Japan. For the $L_{2,3}$ absorption edges of Fe and Co, XMCD spectra were collected at BL25SU [33,45], while XMCD spectra for the $L_{2,3}$ absorption edges of Ir were obtained at BL39XU [46]. Circularly polarized soft X-rays, generated by a twin helical undulator [47], were directed parallel to the applied magnetic field (Fig. 1(c)). XMCD measurements were performed at 77 K under magnetic fields of 1.9 T at BL25SU and 2.4 T at BL39XU, respectively. Notably, the magnetic field was confirmed to be nearly saturated during the measurements (see Fig. S1 in the supplementary materials).

X-ray Absorption Spectroscopy (XAS) spectra were acquired using the total electron yield method, with XMCD spectra derived from the difference between XAS spectra obtained under left and right circularly polarized X-rays. At BL25SU, the XAS spectra for Fe and Co were measured over the energy ranges of 700–751 eV and 772–834 eV, respectively. To reduce noise in the XAS signals, a five-point smoothing process was applied to the spectra. At BL39XU, the spectral ranges for Ir were 11.18–11.27 keV and 12.79–12.87 keV. The compositional gradient within the Fe–Co–Ir film allowed for the collection of 32 distinct XAS spectra at BL25SU and 14 at BL39XU, effectively capturing across different compositions. The sub-millimeter beam spot diameter ensured precise correspondence of each data point to a specific compositional range, thereby enhancing the consistency and reliability of the data.

### C. *Ab-initio* calculations

*Ab-initio* calculations were carried out using the Korringa-Kohn-Rostoker Coherent Potential Approximation (KKR-CPA) method, with the computations executed using the AkaiKKR software [32]. The calculations focused on both the *A*2-disordered and *B*2-ordered structures. For each 1 at% increment in Ir content, spin and orbital magnetic moments, as well as the density of state (DOS) were computed for the *B*2-ordered (Fig. 1(b)) and *A*2-disordered structure to investigate the electronic and magnetic states of the alloy.

## III. RESULTS AND DISCUSSION

### A. XMCD spectra analysis

Fig. 2 illustrates the examples of XAS and XMCD spectra at the $L_3$ and $L_2$ absorption edges of Fe, Co, and Ir in the $(Fe_{75}Co_{25})_{95}Ir_5$ thin film. In the XAS spectra, $\mu^+$ and $\mu^-$, correspond to the absorption for left- and right-circularly polarized X-rays, respectively, with normalization applied using the pre-edge and post-edge regions. The XMCD spectra can be derived from the differences between these spectra. The spectral characteristics align with those reported in previous studies on similar alloy systems [26,41]. The XMCD signal from Ir, as shown in Fig. 2(c), suggests that Ir, despite typically known for its paramagnetic nature, can exhibit measurable magnetization under an external magnetic field. This can be seen by the noticeable XMCD signal. Note that the secondary peak at the $L_2$ absorption edge of Ir, marked by an asterisk in the figure, is likely not intrinsic to Ir and may instead result from diffraction effects related to the MgO(100) substrate or slight variations in lattice constants.

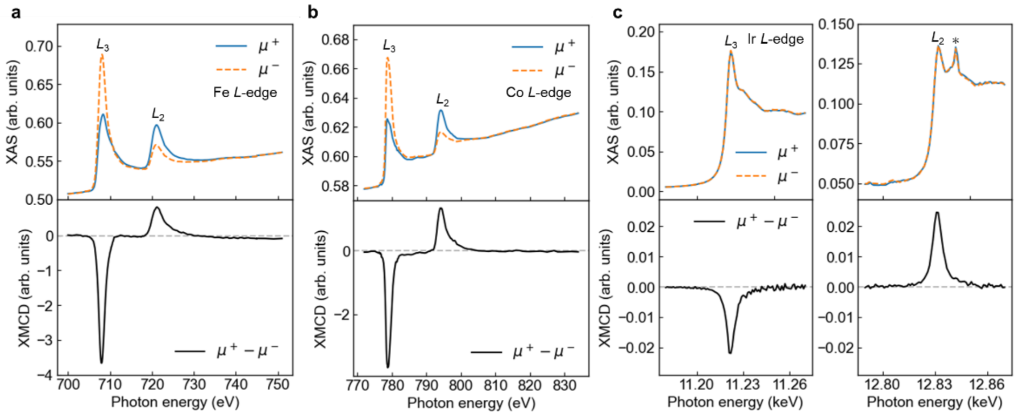

FIG. 2. The XAS (upper panels) and XMCD (lower panels) spectra at the $L_3$ and $L_2$ absorption edges for (a) Fe, (b) Co, and (c) Ir in Fe–Co–Ir alloys, specifically for the composition $(Fe_{75}Co_{25})_{95}Ir_5$ in a compositionally graded film.

## B. Sum-rule analysis for spin and orbital magnetic moments

The analysis of XMCD data reveals contributions from Fe, Co, and Ir to the magnetic properties of the Fe–Co–Ir alloy system. These contributions were quantified using sum-rule analysis, which determines the effective spin magnetic moment ($m_{\mathrm{spin}}^{\mathrm{eff}} = m_{\mathrm{spin}} + 7\langle T_z \rangle$) and the orbital magnetic moment ($m_{\mathrm{orb}}$) for each element [40,41]. The $\langle T_z \rangle$ term, also known as the magnetic dipole term, quantifies the anisotropy in the spin density distribution. It arises from non-spherical contributions to the spin magnetic moment due to spin-orbit interaction and the crystal field. The calculations expressed as follows:

$$m_{spin}^{eff} = -\frac{6p - 4q}{r} n_h \tag{1}$$

$$m_{orb} = -\frac{4q}{3r} n_h \tag{2}$$

where $p$ represents the integrated intensity of the XMCD spectrum at the $L_3$ edge, and $q$ is the integrated intensity over both the $L_3$ and $L_2$ edges. The parameter $r$ denotes the integrated intensity of the white line region in the XAS spectra, adjusted by subtracting a step function. The $n_{\mathrm{h}}$ indicates the number of holes in the 3$d$ and 5$d$ bands, which were determined using ab-initio KKR calculations for each element in the Fe-Co-Ir alloy system. Detailed results, including the dependence of $n_{\mathrm{h}}$ on Ir composition, are provided in Fig. S2 of the supplementary materials.

Prior studies have demonstrated the efficacy of XMCD measurements and the sum-rule analysis for various magnetic materials, such as $L1_0$-FeNi alloys [48] and Fe–Co–Cr atomic-layered films [49]. While $\langle T_z \rangle$ is generally included in the calculation of $m_{\mathrm{spin}}^{\mathrm{eff}}$, its contribution is often negligible in thick films. In this study, the 30 nm-thick Fe–Co–Ir films exhibit negligible $\langle T_z \rangle$ contributions, consistent with previous findings for similar systems [41,50]. Furthermore, it is important to consider that the saturation effect may influence the quantitative accuracy of the sum-rule analysis, particularly in bulk-like films such as the present 30 nm-thick Fe–Co–Ir samples [51]. While the Ir addition is minimal and the perpendicular incidence angle is consistent across all measurement points, saturation effects could still vary depending on the intrinsic X-ray penetration depth and electron escape depth, which may differ with composition. Although angular-dependent measurements are required to address these effects quantitatively, the present study is limited to a single perpendicular geometry. As such, while the saturation effect correction does not affect the relative comparison of elemental magnetic moment variations, we note that this should be considered for a precise discussion of absolute magnetic moment values.

Fig. 3 shows the experimental results for the spin and orbital magnetic moments of Fe, Co, and Ir, plotted as functions of Ir concentration. The sum-rule analysis reveals a positive correlation between Ir content and the magnetic moments of all three elements. The slopes of the spin and orbital moments demonstrate minimal differences, highlighting the significant contribution of each element to the overall magnetization of the alloy. The linear fits of our experimental data provide further insight. Fe, the predominant element, shows the most significant increase in both spin and orbital moments—1.07 and 1.41 times those of $Fe_{75}Co_{25}$, respectively. Co exhibits a moderate increase, with its spin and orbital moments rising to 1.12 and 1.08 times their initial values. Notably, Ir shows a pronounced enhancement, with its spin moment increasing 1.07 times and its orbital moment to 1.53 times their original values, emphasizing its crucial role in enhancing the overall magnetic properties. It should be noted that the data point for 1 at% Ir was excluded from the linear fitting for the Ir element because the signal intensity of the Ir spectrum at such low concentrations was weak, resulting in low reliability. The scatter in the measurement data can be attributed to challenges in thin-film experiments, such as the use of 30 nm-thick films and short signal accumulation times for XMCD measurements, particularly for low-signal elements. Nevertheless, the trends observed from the linear fits allow us to draw meaningful conclusions regarding Ir effect on magnetic behavior.

Interestingly, Ir, which is typically paramagnetic, exhibits measurable magnetic moments when alloyed with Fe and Co, supporting prior reports of Ir-induced magnetization in similar systems [21,26–29]. For example, Iwasaki *et al.* [21] demonstrated that adding up to 8 at% of Ir concentration to Fe–Co alloys can enhance saturation magnetization, a result supported by *ab-initio* calculations. In contrast, Krishnamurthy *et al.* [27] observed a decrease in overall magnetic moments in Fe–Ir alloys with Ir additions up to 17 at%. and Jiao *et al.* [29] similarly reported a reduction of the total magnetization for Co–Ir alloys when the Ir concentration was increased from 8.9 to 18.9 at%. Our results suggest that small amount of Ir can enhance the magnetic moments of individual elements in Fe–Co–Ir alloys. However, as Ir content increases, the overall magnetization tends to decrease, likely due to the weak magnetic contribution of Ir. Additionally, previous studies may show varying trends because of factors such as non-single-crystal samples or differences in the ranges of Ir concentrations investigated. It is also important to note that the scatter observed in the measurement plots is likely due to challenges inherent in thin-film experiments, including the use of 30 nm-thick films and shorter signal accumulation times required to capture multiple data points to analysis the trend of Ir addition. These limitations affected the precision of XMCD measurements, particularly for elements with low signal strength. Nevertheless, the linear fits still reveal clear trends, enabling us to draw meaningful conclusions regarding the effect of Ir on the magnetic properties.

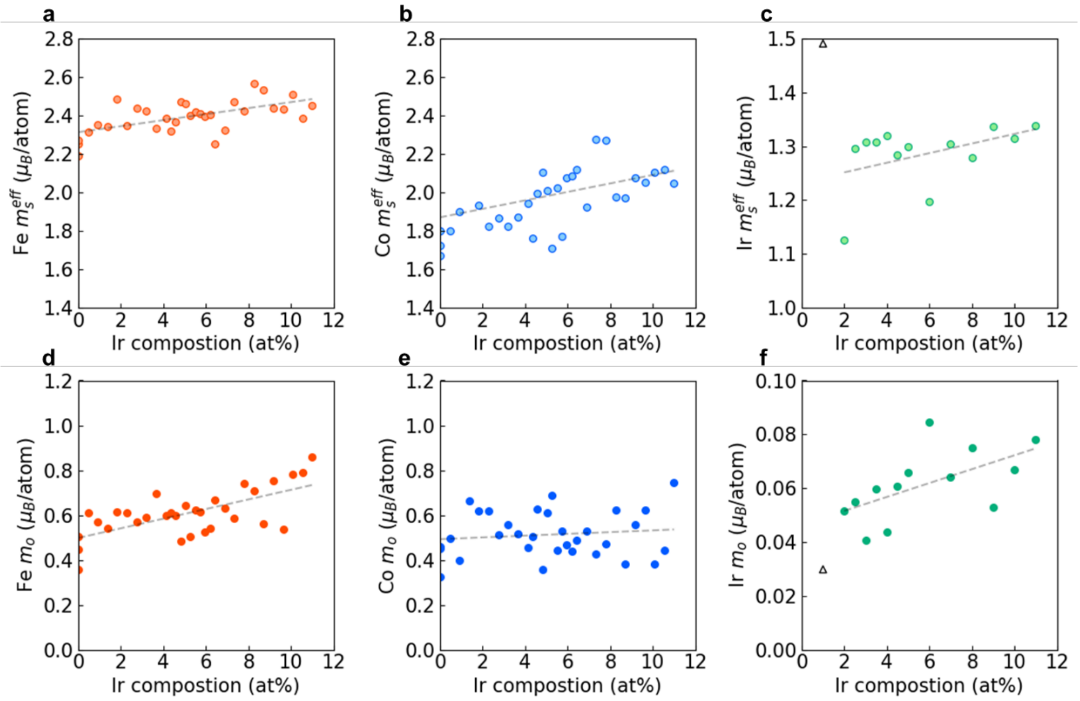

FIG. 3. Experimental results of spin and orbital magnetic moments for each element of (a, d) Fe, (b, e) Co, and (c, f) Ir, showing their variation with Ir concentration. (a), (b), and (c) display the spin magnetic moments. Also, (d), (e), and (f) illustrate the orbital magnetic moments. To illustrate the trends, linear approximations obtained using the least squares method have been included for each element.

Fig. 4 presents the theoretical spin and orbital magnetic moments of Fe, Co, and Ir for both *A*2-disordered and *B*2-ordered structures as functions of Ir concentration. Since prior studies [24], have confirmed the presence of *B*2-ordered structure in Fe–Co–Ir alloys through XRD measurements, we extended our theoretical calculations to include both *A*2 and *B*2 structures to fully capture the effects of Ir addition. The results show that the magnetic moments increase with Ir concentration in both structures, but the *B*2 structure yields consistently higher magnetic moments than the *A*2 structure.

In the *B*2-ordered structure, Fe demonstrates a larger increase, with the spin moment increasing by 1.12 times and the orbital moment by 1.39 times as Ir content increases from 0% to 11 at%. Co exhibits a more modest increase, with the spin and orbital moments rising by 1.07 and 1.25 times, respectively. Ir shows the most notable enhancement, with its spin moment increasing by 1.11 times and its orbital moment showing a remarkable 8.28-fold increase. These results highlight the critical role of Ir in enhancing the magnetic properties, especially in the B2 structure.

Both experimental and theoretical data consistently indicate that Ir addition enhances the magnetic moments of Fe, Co, and Ir, with the largest effects seen in Fe and Ir. Although we performed XMCD measurements on samples with an expected structural transition from *A*2 to *B*2 with at least 2.1% Ir addition, the changes were too subtle to definitively confirm the transition in this experiment. This limitation should be carefully considered when interpreting the results, as it may affect the ability to fully verify the influence of the *B*2 structure on the magnetic moments. Nonetheless, the theoretical findings highlight the potential impact of the *B*2 ordering on the magnetic properties.

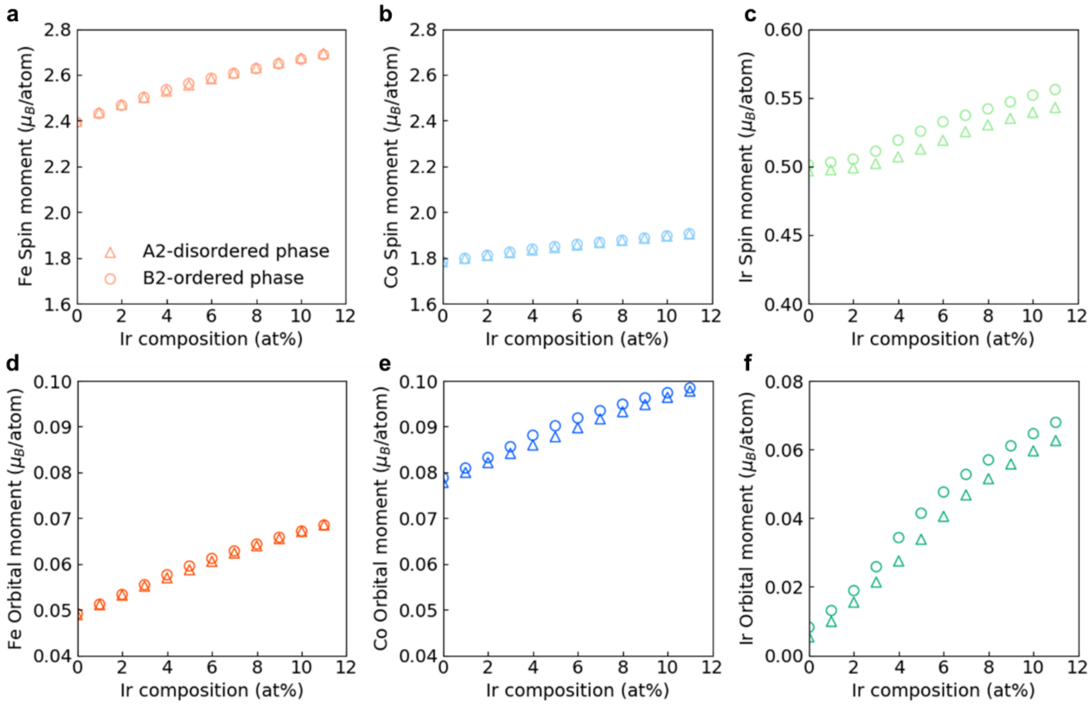

FIG. 4. Theoretical calculations of spin and orbital magnetic moments for each element: (a, d) Fe, (b, e) Co, and (c, f) Ir, with variation in Ir composition. (a), (b), and (c) display the spin magnetic moments, while (d), (e), and (f) illustrate the orbital magnetic moments. The symbols △ and ○ represent the data for the *A*2-disordered phase and *B*2-ordered phase, respectively.

### C. Total magnetic moments

Fig. 5 compares the experimental and theoretical results for the spin and orbital magnetic moments of Fe, Co, and Ir, derived from the trends from Fig. 3. The addition of Ir enhances the magnetic moments of all three elements in both experimental and theoretical datasets. However, significant differences are observed in the absolute values, particularly in the orbital magnetic moments, which are higher in the experimental results than in theoretical calculations.

This discrepancy can be partly explained by the fact that the theoretical calculations assume a perfectly *B*2-ordered structure, while the experimental films exhibit a *B*2 ordering degree less than

1 [24]. Additionally, the theoretical models tend to underestimate spin-orbit coupling and do not fully incorporate surface and interface effects, particularly in thin films or nanoscale structures, potentially leading to an underestimation of orbital magnetic moments, as noted in previous studies [43,43]. The delocalization of electrons in 5*d* elements in Ir and the inadequate consideration of electron-electron interactions may further contribute to these differences [28]. Importantly, the results show that the increase in magnetic moments with Ir addition is primarily driven by the orbital moments rather than the spin moments. This observation aligns with findings by Imada *et al.*, who demonstrated that strong spin-orbit interactions in 5*d* elements, such as Pt, can localize 3*d* electrons and significantly enhance the orbital angular momentum contribution [52].

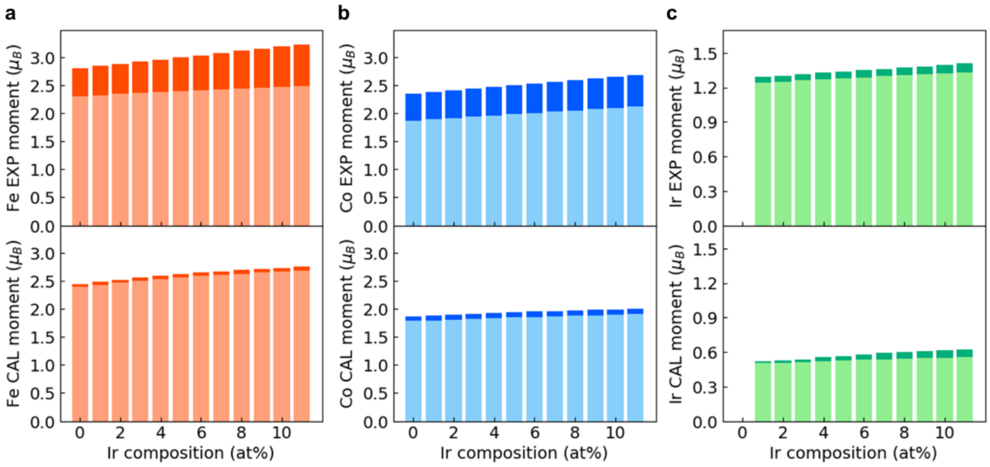

FIG. 5. Comparison of experimental (upper panel) and theoretical (lower panel) results of spin and orbital magnetic moments for each element of (a) Fe, (b) Co, and (c) Ir.

The analysis of the density of states (DOS) for the *d*-orbitals of Fe, Co, and Ir atoms in Fe–Co–Ir alloys, performed using *ab-initio* calculations, offers critical insights into the influence of Ir incorporation on the electronic and magnetic properties within the *B*2-ordered structure. As shown in Fig. 6, the DOS for each element at 3, 7, and 10 at% Ir concentrations reveals distinct shifts in particularly at the Fermi level. These shifts are accompanied by a sharpening of DOS peaks for Fe and Co, indicating increased electron localization, with Fe showing a stronger interaction with Ir due to enhanced spin-orbit coupling (SOC) from the Ir 5*d* electrons [53,54]. This aligns with the observed increase in Fe orbital magnetic moment, underscoring the role of Ir in tuning the magnetic behavior. In contrast, Ir DOS shifts with increasing concentration, with majority spin states moving to lower energies and a rise in DOS intensity, suggesting enhanced spin polarization [28,55]. XMCD results confirm these theoretical changes, showing induced magnetism in Ir due to 3*d*-5*d* exchange interactions with ferromagnetic Fe and Co. This interaction amplifies the overall magnetic properties, demonstrating the synergistic effect of Ir with Fe and Co [27, 52].

Our study reveals a consistent increase in the magnetic moment within the 0–11 at% Ir concentration range for $Fe_{75}Co_{25}$ alloys. Ir doping enhances electron localization, which plays a key role in increasing the orbital magnetic moments of Fe, Co, and Ir. This complex interplay between SOC and electron localization advances our understanding of magnetic behavior in these alloys and sets the stage for future quantitative analyses. While higher Ir concentrations in other systems have been associated with reduced magnetic moments due to antiferromagnetic exchange interactions [27,50], further investigations beyond the 11% Ir concentration could shed light on the limits of this effect. Moreover, exploring the correlation between magnetic moments, electronic states, and other physical properties could provide deeper insights into the effects of Ir doping and SOC. These efforts will help further elucidate the underlying mechanisms driving the magnetic behavior of these alloys.

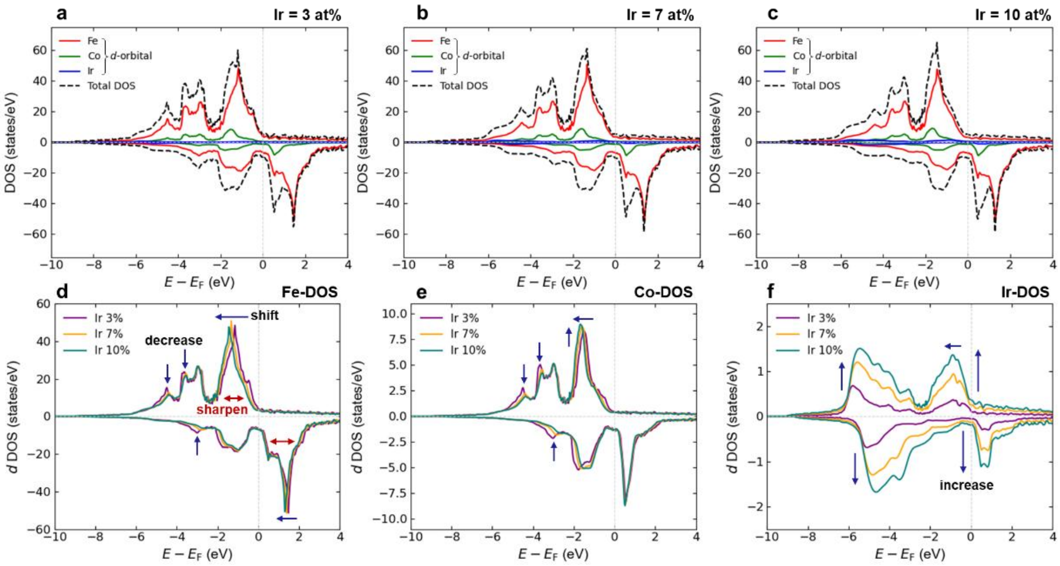

FIG. 6 Density of states (DOS) and element-resolved *d*-orbital and total DOS per atom in Fe–Co–Ir alloys at varying Ir concentrations: (a) 3 at%, (b) 7 at%, and (c) 10 at%. Panels (d), (e), and (f) illustrate the *d*-orbital contributions to the DOS for Fe, Co, and Ir, respectively.

## IV. CONCLUSIONS

This study quantitively investigated the influence of Ir doping on element-specific magnetic moments of Fe–Co–Ir alloys using soft and hard X-ray Magnetic Circular Dichroism (XMCD) technique on composition-spread films, combined with *ab-initio* calculations. A compositionally graded thin film of $(Fe_{75}Co_{25})_{100-x}Ir_x$ ($x$ = 0–11 at%) was fabricated using a combinatorial sputtering technique, enabling systematic compositional analysis.

High-throughput XMCD measurements revealed significant enhancements in the orbital magnetic moments of Fe and Ir due to Ir doping, with Fe increasing to 1.41 times and Ir to 1.53 times their original values. Theoretical calculations supported these findings, attributing the enhancements to increased electron localization and augmented spin-orbit coupling. The interaction between the 5*d* electrons of Ir and the 3*d* electrons of Fe and Co was identified as a key factor, facilitating a shift in electronic states to lower energy levels, thereby amplifying the orbital contributions to magnetic moments.

Theoretical calculations of the density of states (DOS) revealed that Ir addition shifts the Fe and Co electronic states to lower energy levels, resulting in enhanced magnetic moments, primarily through increased orbital contributions. The calculations also showed that the magnetic moments in the *B*2-ordered crystal structure are larger than those in the *A*2-disordered structure, strongly supporting the experimental findings. This validates that the *B*2-ordered phase contributes to the observed magnetization enhancements. The pronounced increase in orbital magnetic moments with Ir doping further underscores the importance of spin-orbit coupling in this system. These trends suggest that Ir serves as a catalyst for boosting magnetic properties, particularly through its interaction with Fe, which exhibited the largest increases in magnetic moments in both experimental and theoretical data. This reinforced the critical role of Ir in improving the magnetic behavior of the alloy.

Overall, Ir doping effectively enhances the magnetic characteristics of Fe–Co–Ir alloys, leading to significant increases in both spin and orbital contributions to the overall magnetization. The strong agreement between experimental results and theoretical models reinforces the reliability of these findings, offering valuable insights into the electronic and magnetic interactions within these alloys. This study not only provides essential insights into the interplay of spin-orbit coupling and magnetic moments in 5*d*-doped ferromagnetic alloys but also establishes a clear foundation for designing high-performance ferromagnetic materials for advanced technological applications.

## ACKNOWLEDGEMENTS

The XMCD experiments at BL25SU and BL39XU were carried out under the approval of SPring-8 (Proposals: 2022A1027, 2022B1004, and 2023A1179). Also, this study was supported in part by JST-CREST (Grant No. JPMJCR21O1) and JST/ACT-X (Grant No. JPMJAX22AL), and Japan Society for the Promotion of Science, JSPS (KAKENHI: Grants No. 21H04656, 22K14590, 23K13636).

## References

[1] O. Gutfleisch, M. A. Willard, E. Brück, C. H. Chen, S. G. Sankar, and J. P. Liu, *Adv. Mater.* **23**, 821 (2011).

[2] J. M. Silveyra, E. Ferrara, D. L. Huber, and T. C. Monson, *Science* **362**, eaao0195 (2018).

[3] W. D. Callister Jr. and D. G. Rethwisch, *Materials Science and Engineering: An Introduction* (John Wiley & Sons, 2020).

[4] J. M. D. Coey, *Magnetism and Magnetic Materials* (Cambridge University Press, 2010).

[5] A. Williams, V. Moruzzi, A. Malozemoff, and K. Terakura, *IEEE Trans. Magn.* **19**, 5 (1983).

[6] Z. J. Huba, K. J. Carroll, and E. E. Carpenter, *J. Appl. Phys.* **109**, 7 (2011).

[7] D. M. Clifford, C. E. Castano, A. J. Lu, and E. E. Carpenter, *J. Mater. Chem. C* **3**, 11029 (2015).

[8] F. Sánchez-De Jesús, A. M. Bolarín-Miró, C. A. Cortés Escobedo, G. Torres-Villaseñor, and P. Vera-Serna, *J. Metallurgy* **2016**, 8347063 (2016).

[9] A. Najafi and K. Nematipour, *J. Supercond. Nov. Magn.* **30**, 2647 (2017).

[10] M. Matsui, K. Sato, and K. Adachi, *J. Phys. Soc. Jpn.* **35**, 419 (1973).

[11] S. K. Arora, H.-C. Wu, R. J. Choudhary, I. V. Shvets, O. N. Mryasov, H. Yao, and W. Y. Ching, *Phys. Rev. B* **77**, 134443 (2008).

[12] H. Ü. Kurt, K. Rode, M. Venkatesan, P. Stamenov, and J. M. D. Coey, *Phys. Rev. B* **83**, 020405 (2011).

[13] R. J. Snow, H. Bhatkar, A. T. N'Diaye, E. Arenholz, and Y. U. Idzerda, *Appl. Phys. Lett.* **112**, 7 (2018).

[14] M. Sicot, S. Andrieu, F. Bertran, and F. Fortuna, *Phys. Rev. B* **72**, 144414 (2005).

[15] N. J. Szymanski, B. Rendy, Y. Fei, R. E. Kumar, T. He, D. Milsted, M. J. McDermott, *et al.*, *Nature* **624**, 86 (2023).

[16] A. Agrawal and A. Choudhary, *APL Mater.* **4**, 5 (2016).

[17] R. Ramprasad, R. Batra, G. Pilania, A. Mannodi-Kanakkithodi, and C. Kim, *npj Comput. Mater.* **3**, 54 (2017).

[18] W. Chaikittisilp, Y. Yamauchi, and K. Ariga, *Adv. Mater.* **34**, 2107212 (2022).

[19] D. Furuya, T. Miyashita, Y. Miura, Y. Iwasaki, and M. Kotsugi, *Sci. Technol. Adv. Mater. Methods* **2**, 280 (2022).

[20] R. M. Rowan-Robinson, Z. Leong, S. Carpio, C. Oh, and N. A. Morley, *AIP Adv.* **14**, 1 (2024).

[21] Y. Iwasaki, R. Sawada, E. Saitoh, and M. Ishida, *Commun. Mater.* **2**, 31 (2021).

[22] J. Nelson and S. Sanvito, *Phys. Rev. Mater.* **3**, 104405 (2019).

[23] P. Singh, T. Del Rose, A. Palasyuk, and Y. Mudryk, *Chem. Mater.* **35**, 6304 (2023).

[24] R. Toyama, S. Kokado, K. Masuda, Z. Li, V. K. Kushwaha, T. T. Sasaki, *et al.*, *Phys. Rev. Mater.* **7**, 084401 (2023).

[25] R. Toyama, W. Zhou, and Y. Sakuraba, *Phys. Rev. B* **109**, 054415 (2024).

[26] S. Miwa, T. Nozaki, M. Tsujikawa, M. Suzuki, T. Tsukahara, T. Kawabe, *et al.*, *Phys. Rev. B* **99**, 184421 (2019).

[27] V. V. Krishnamurthy, M. Suzuki, N. Kawamura, T. Ishikawa, and Y. Kohori, *Physica B* **312**, 647 (2002).

[28] V. V. Krishnamurthy, D. J. Singh, N. Kawamura, M. Suzuki, and T. Ishikawa, *Phys. Rev. B* **74**, 064411 (2006).

[29] J. Jiao, T. Wang, T. Ma, Y. Wang, and F. Li, *Nanoscale Res. Lett.* **12**, 1 (2017).

[30] T. Goto, J. Takahashi, M. Nakamura, T. Hirose, K. Watanabe, and H. Yoshida, *J. Magn. Magn. Mater.* **226**, 1656 (2001).

[31] V. Kashid, T. Schena, B. Zimmermann, Y. Mokrousov, S. Blügel, V. Shah, and H. G. Salunke, *Phys. Rev. B* **90**, 054412 (2014).

[32] H. Akai, *J. Phys. Soc. Jpn.* **51**, 468 (1982).

[33] S. Suga, S. Imada, A. Yamasaki, S. Ueda, T. Muro, and Y. Saitoh, *J. Magn. Magn. Mater.* **233**, 60 (2001).

[34] W. Grange, I. Galanakis, M. Alouani, M. Maret, J. P. Kappler, and A. Rogalev, *Phys. Rev. B* **62**, 1157 (2000).

[35] S. Imada, T. Muro, T. Shishidou, S. Suga, H. Maruyama, K. Kobayashi, *et al.*, *Phys. Rev. B* **59**, 8752 (1999).

[36] H. Koinuma and I. Takeuchi, *Nat. Mater.* **3**, 429 (2004).

[37] M. L. Green, I. Takeuchi, and J. R. Hattrick-Simpers, *J. Appl. Phys.* **113**, 23 (2013).

[38] A. G. Kusne, T. Gao, A. Mehta, L. Ke, M. C. Nguyen, K. M. Ho, *et al.*, *Sci. Rep.* **4**, 6367 (2014).

[39] A. Ludwig, *NPJ Comput. Mater.* **5**, 70 (2019).

[40] P. Carra, B. T. Thole, M. Altarelli, and X. Wang, *Phys. Rev. Lett.* **70**, 694 (1993).

[41] C. T. Chen, Y. U. Idzerda, H.-J. Lin, N. V. Smith, G. Meigs, E. Chaban, G. H. Ho, E. Pellegrin, and F. Sette, *Phys. Rev. Lett.* **75**, 152 (1995).

[42] B. T. Thole, P. Carra, F. Sette, and G. van der Laan, *Phys. Rev. Lett.* **68**, 1943 (1992).

[43] G. van der Laan and A. I. Figueroa, *Coord. Chem. Rev.* **277**, 95 (2014).

[44] R. Toyama, V. K. Kushwaha, T. T. Sasaki, Y. Iwasaki, T. Nakatani, and Y. Sakuraba, *APL Mater.* **11**, 10 (2023).

[45] T. Nakamura, T. Muro, F. Z. Guo, T. Matsushita, T. Wakita, T. Hirono, *et al.*, *J. Electron Spectrosc. Relat. Phenom.* **144**, 1035 (2005).

[46] M. Suzuki, N. Kawamura, M. Mizumaki, Y. Terada, T. Uruga, A. Fujiwara, *et al.*, *J. Phys. Conf. Ser.* **430**, 012017 (2013).

[47] T. Hara, K. Shirasawa, M. Takeuchi, T. Seike, Y. Saito, T. Muro, and H. Kitamura, *Nucl. Instrum. Methods Phys. Res. A* **498**, 496 (2003).

[48] M. Kotsugi, M. Mizuguchi, S. Sekiya, M. Mizumaki, T. Kojima, T. Nakamura, *et al*., *J. Magn. Magn. Mater.* **326**, 235 (2013).

[49] T. Nishio, M. Yamamoto, T. Ohkochi, D. Nanasawa, A. L. Foggiatto, and M. Kotsugi, *Sci. Technol. Adv. Mater. Methods* **2**, 345 (2022).

[50] D. Weller, J. Stöhr, R. Nakajima, A. Carl, M. G. Samant, C. Chappert, *et al*., *Phys. Rev. Lett.* **75**, 3752 (1995).

[51] T. Nakamura, Y. Kanno, and S. Takagi., *Phys. Rev. B* **51**.13 (1995): 8446.

[52] A. Langenberg, K. Hirsch, A. Ławicki, V. Zamudio-Bayer, M. Niemeyer, P. Chmiela, et al., *Phys. Rev. B* **90**, 184420 (2014).

[53] M. Bouhassoune, I. L. Fernandes, S. Blügel, and S. Lounis, *New J. Phys.* **21**, 063015 (2019).

[54] F. Nickel, S. Meyer, and S. Heinze, *Phys. Rev. B* **107**, 174430 (2023).

[55] D. Odkhuu, W. S. Yun, S. H. Rhim, and S. C. Hong, *Appl. Phys. Lett.* **98**, 15 (2011).